Miner Deposita (2006) 41: 160–178
DOI 10.1007/s00126-006-0050-1

ARTICLE

Evandro L. Klein · Chris Harris · Christophe Renac · André Giret · Candido A. V. Moura · Kazuo Fuzikawa

Fluid inclusion and stable isotope (O, H, C, and S) constraints on the genesis of the Serrinha gold deposit, Gurupi Belt, northern Brazil

Received: 24 February 2005 / Accepted: 25 January 2006 / Published online: 23 March 2006

Abstract The Serrinha gold deposit of the Gurupi Belt, northern Brazil, belongs to the class of orogenic gold deposits. The deposit is hosted in highly strained graphitic schist belonging to a Paleoproterozoic (~2,160 Ma) metavolcano-sedimentary sequence. The ore-zones are up to 11 m thick, parallel to the regional NW–SE schistosity, and characterized by quartz-carbonate-sulfide veinlets and minor disseminations. Textural and structural data indicate that mineralization was syn- to late-tectonic and post-metamorphic. Fluid inclusion studies identified early CO_2 (CH_4-N_2) and CO_2 (CH_4-N_2)-H_2O-NaCl inclusions that show highly variable phase ratios, CO_2 homogenization, and total homogenization temperatures both to liquid and vapor, interpreted as the product of fluid immiscibility under fluctuating pressure conditions, more or less associated with postentrapment modifications. The ore-bearing fluid typically has 18–33mol% of CO_2, up to 4mol% of N_2, and less than 2mol% of CH_4 and displays moderate to high densities with salinity around 4.5wt% NaCl equiv. Mineralization occurred around 310 to 335°C and 1.3 to 3.0 kbar, based on fluid inclusion homogenization temperatures and oxygen isotope thermometry with estimated oxygen fugacity indicating relatively reduced conditions. Stable isotope data on quartz, carbonate, and fluid inclusions suggest that veins formed from fluids with $\delta^{18}O_{H2O}$ and δD_{H2O} (310–335°C) values of +6.2 to +8.4‰ and −19 to −80‰, respectively, which might be metamorphic and/or magmatic and/or mantle-derived. The carbon isotope composition ($\delta^{13}C$) varies from −14.2 to −15.7‰ in carbonates; it is −17.6‰ in fluid inclusion CO_2 and −23.6‰ in graphite from the host rock. The $\delta^{34}S$ values of pyrite are −2.6 to −7.9‰. The strongly to moderately negative carbon isotope composition of the carbonates and inclusion fluid CO_2 reflects variable contribution of organic carbon to an originally heavier fluid (magmatic, metamorphic, or mantle-derived) at the site of deposition and sulfur isotopes indicate some oxidation of the originally reduced fluid. The deposition of gold is interpreted to have occurred mainly in response to phase separation and fluid-rock interactions such as CO_2 removal and desulfidation reactions that provoked variations in the fluid pH and redox conditions.

Keywords Fluid inclusion · Stable isotope · Gold · Gurupi belt · Paleoproterozoic

Editorial handling: H. Frimmell

E. L. Klein (✉)
CPRM/Geological Survey of Brazil,
Av. Dr. Freitas, 3645,
Belém-PA, CEP: 66095-110, Brazil
e-mail: eklein@be.cprm.gov.br
Tel.: +55-91-32768577
Fax: +55-91-32764020

C. Harris · C. Renac · A. Giret
Département de Géologie, Université Jean Monnet,
23, rue du Docteur Paul Michelon,
Saint Etienne 42000,
Cedex 2, France

C. Harris
Department of Geological Sciences,
University of Cape Town,
Rondebosch 7700, South Africa

C. A. V. Moura
Laboratório de Geologia Isotópica, Pará-Iso,
Universidade Federal do Pará,
CP 1611,
Belém-PA, CEP: 66075-900, Brazil

K. Fuzikawa
CDTN/CNEN, Rua Mario Werneck s/n,
Cidade Universitária,
Belo Horizonte-MG, CEP: 30270-010, Brazil

Introduction

The Serrinha deposit is located in the Gurupi Belt in northern Brazil (Fig. 1). It is part of a group of gold deposits and prospects (Cachoeira, Chega Tudo, Cipoeiro, and Montes Áureos) and minor occurrences that were intermittently developed by different mining companies. Geologic and/or genetic information is available for Cachoeira (Klein et al. 2005a), Chega Tudo-Cipoeiro

(Torresini 2000), and Montes Áureos (Yamaguti and Villas 2003). The geologic framework and tectonic evolution of the Gurupi Belt is reasonably outlined (Klein et al. 2005c, and references therein) as well. However, neither the geologic nor the genetic aspects of the Serrinha deposit were described to date and the discussion of these two aspects is the intention of this paper. A summary of the geologic context and characteristics of gold mineralization in the Gurupi Belt is presented and we provide new data on the geology of the Serrinha deposit based on drill core and petrographic information, fluid inclusion, and reconnaissance stable isotope (O, H, C, and S) studies on hydrothermal minerals. The results allow us to place constraints on the temperature, pressure, composition, and redox conditions of the ore-bearing fluid and to discuss possible sources for ore fluids and solutes.

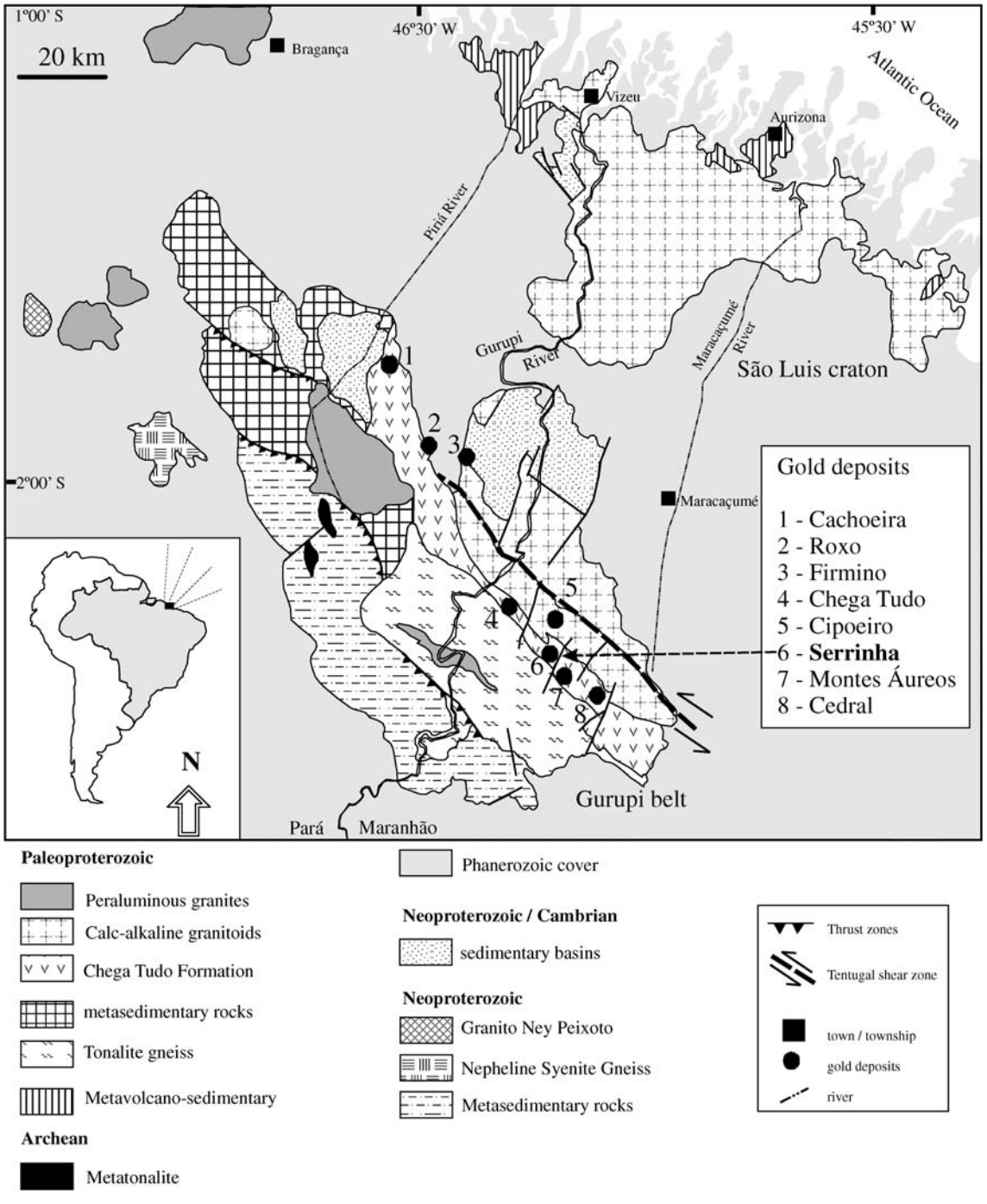

Fig. 1 Geological map of the São Luís craton and Gurupi belt showing the location of Serrinha and other gold deposits

Geologic setting

The Gurupi Belt borders the south–southwestern portion of the São Luis Craton (Fig. 1). The craton area is composed of juvenile calc-alkaline granitoids and metavolcano-sedimentary sequences that evolved mainly between 2,240 and 2,149 Ma (Klein and Moura 2001, 2003; Klein et al. 2005b) and of younger S-type granitoids of about 2,090 Ma (Palheta 2001). The cratonization is estimated to have occurred around 1,900 Ma as suggested by K–Ar cooling age (see Klein and Moura 2003 for primary references).

The Gurupi Belt comprises NNW–SSE-trending metavolcano-sedimentary and sedimentary sequences, gneisses, and different generations of felsic intrusive rocks. The volcano-sedimentary sequence (Chega Tudo Formation) consists of schists derived from an alternation of felsic to mafic volcanic and clastic sedimentary rocks that were deformed and metamorphosed under subgreenschist to lower-amphibolite facies conditions. These schists show a NNW–SSE striking foliation that dip at moderate to high angles predominantly to the southwest. Felsic metavolcanic rocks have zircon ages between 2,148 and 2,160 Ma (Klein and Moura 2001). Metasedimentary sequences are ascribed to the Gurupi Group (Fig. 1) whose stratigraphic age is still unknown, but tentatively positioned in the Paleoproterozoic Age (minimum age 2,159 Ma). Orthogneisses of tonalite-granodiorite composition (Itapeva Complex) and peraluminous granites are tectonically intercalated with the supracrustal rocks. The gneisses are banded, middle- to upper-amphibolite facies rocks that underwent incipient migmatization. A tonalitic protolith of the gneisses yielded a U-Pb ID-TIMS zircon age of 2,167± 2.5 Ma (Klein et al. 2005c). Granitoids of variable chemical affinities and ages either intruded or are tectonically intercalated with the supracrustal and gneissic sequences. A calc-alkaline monzogranite body gave a zircon age of 2,159±13 Ma (Palheta 2001). Peraluminous granitoids are relatively widespread and show variable effects of deformation depending on their position relative to shear zones. Zircon ages of these peraluminous granites vary between 2,061 and 2,100 Ma, whereas some inherited zircon grains and Nd isotope information show that both Paleoproterozoic and Archean crustal protoliths were involved in the source of the magmas (Palheta 2001; Klein et al. 2005c). The above units of the Gurupi Belt and the São Luis Craton are interpreted to be part of a Paleoproterozoic orogen having a protracted evolution between 2,240 and 2,060 Ma. Two peaks of geologic activity are recorded by the voluminous production of subduction-related calc-alkaline rocks at 2,160–2,150 Ma (accretionary phase) and by the emplacement of peraluminous granites at 2,100–2,080 Ma (collision phase) (Palheta 2001; Klein et al. 2005b,c). This Paleoproterozoic scenario, including rock assemblages, tectonic setting, and chronology of events, correlates well with what is described for the Birimian terranes affected by the Paleoproterozoic Eburnean orogeny in the West African Craton (Klein et al. 2005b,c, and references therein).

A Neoproterozoic orogen developed in the southern portion of the region. This episode is not fully described yet due to the scarcity of geologic and geochronological

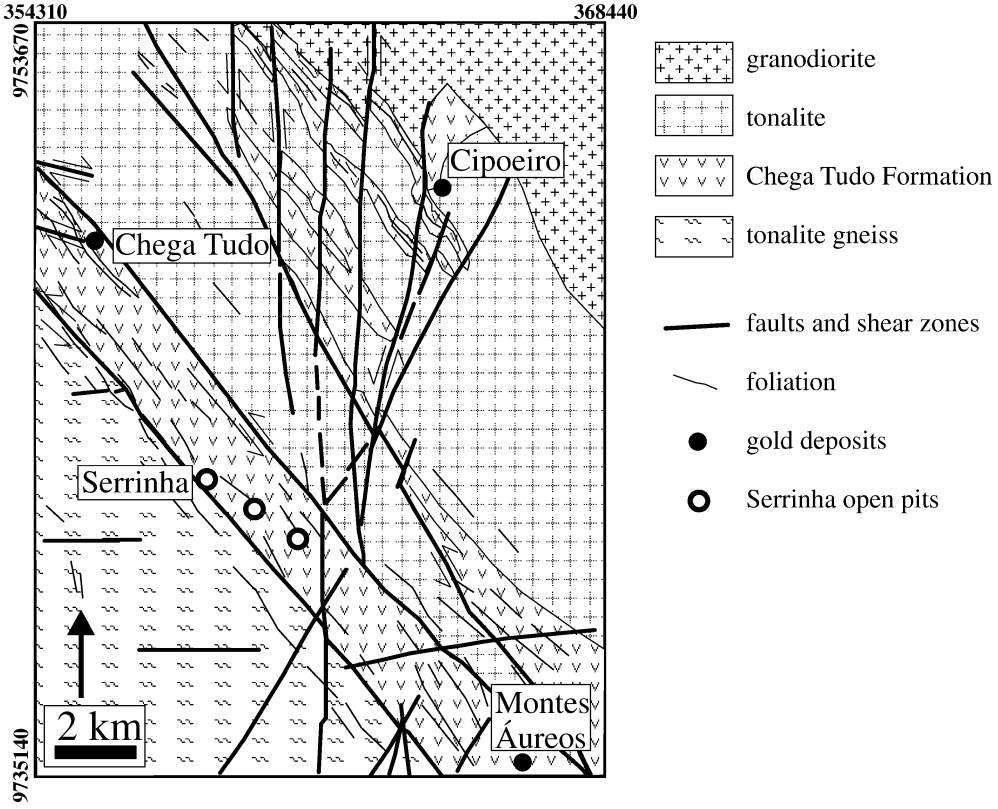

Fig. 2 Geological map of the central portion of the Gurupi belt in the Serrinha area. Adapted from Ribeiro (2002)

information. The available data show that two intrusions probably mark the opening and closure of an orogenic basin, which might be either an oceanic or a continental rift basin. These intrusions are the Boca Nova nepheline syenite of 732 Ma (Klein et al. 2005c) and the post-tectonic Ney Peixoto peraluminous granite of 549 Ma (Palheta 2001), respectively. Furthermore, mineral Rb–Sr and K–Ar ages of most of the rock units in the Gurupi Belt are in the 520–670 Ma range (Hurley et al. 1968; Almeida et al. 1968; Villas 1982; Klein and Moura 2003), reinforcing the influence of the Neoproterozoic events.

Small extensional sedimentary basins formed over the rocks of the São Luis Craton and the Gurupi Belt (Fig. 1). These basins are filled with continental detrital sedimentary rocks (arkose, pelites, and conglomerates) that show a weak foliation and large open folds and underwent localized anchimetamorphism.

Gold mineralization in the Gurupi Belt

The gold deposits and showings in the Gurupi Belt (Fig. 1) are mostly hosted in metavolcano-sedimentary rocks belonging to the Chega Tudo Formation and subordinately in sheared calc-alkaline tonalites, both having ages between 2,150 and 2,170 Ma. These sequences are interpreted (Klein et al. 2005c) as accretionary assemblages and related to a Paleoproterozoic orogen. Furthermore, the deposits are located close to the interpreted boundary zone between the accretionary and collisional assemblages of this orogen (Klein et al. 2005c), i.e., in a continental margin.

All deposits show strong structural control, being related to the major Tentugal shear zone (Fig. 1), which is a sinistral strike-slip structure characterized by a 15- to 30-km-wide corridor of deformed rocks that lie within the boundary zone between the São Luis Craton and the Gurupi Belt. Carbon-bearing schists, metapelites, and felsic metavolcanic rocks are the rocks that concentrated most of the strain due to their rheologic contrast with respect to the coarse-grained schists and gneisses that crop out to the south–southwest and the tonalites that crop out to the north (Ribeiro 2002). Most deposits are located in sheared rocks that parallel the regional NW–SE trend of the Tentugal shear zone and a few (e.g., Cipoeiro) are located in splays geometrically related to the shear zone (Figs. 1 and 2). In the Serrinha area, this NW–SE-trending corridor is broadly linear and limited by north–south trending faults (Ribeiro 2002).

Structural and textural relationships indicate that hydrothermal gold mineralization postdates the regional metamorphic peak and is syn- to late-tectonic with respect to the development of the Tentugal shear zone. The absolute timing of gold mineralization in the Gurupi Belt is not yet constrained. Geologic and preliminary Pb isotope data strongly suggest that mineralization occurred between 2,000 and 2,060 Ma, at least in the Cachoeira deposit (Klein et al. 2005a). This age interval is roughly coincident with the range of ages accepted for gold mineralization associated with the Birimian sequences of the West African Craton (Marcoux and Milési 1993; Oberthür et al. 1998), which shows a tectonic context similar to that proposed for the Paleoproterozoic in the Gurupi Belt/São Luís Craton. These West African Paleoproterozoic gold deposits are considered to be examples of the class of orogenic gold deposits (Groves et al. 1998). In the Gurupi Belt, at least Montes Áureos (Yamaguti and Villas 2003) and Cachoeira (Klein et al. 2005a) are interpreted to belong to this class.

Updated reserves and historical production for individual deposits of the Gurupi Belt are still unknown. Early evaluations (A. S. Almeida, unpublished report) report 7.2, 3.3, and 4.6 tonnes Au of primary, supergene, and alluvial gold, respectively, totaling resources of 15.1 tonnes Au for Serrinha and Chega Tudo. Also, estimates for the historical

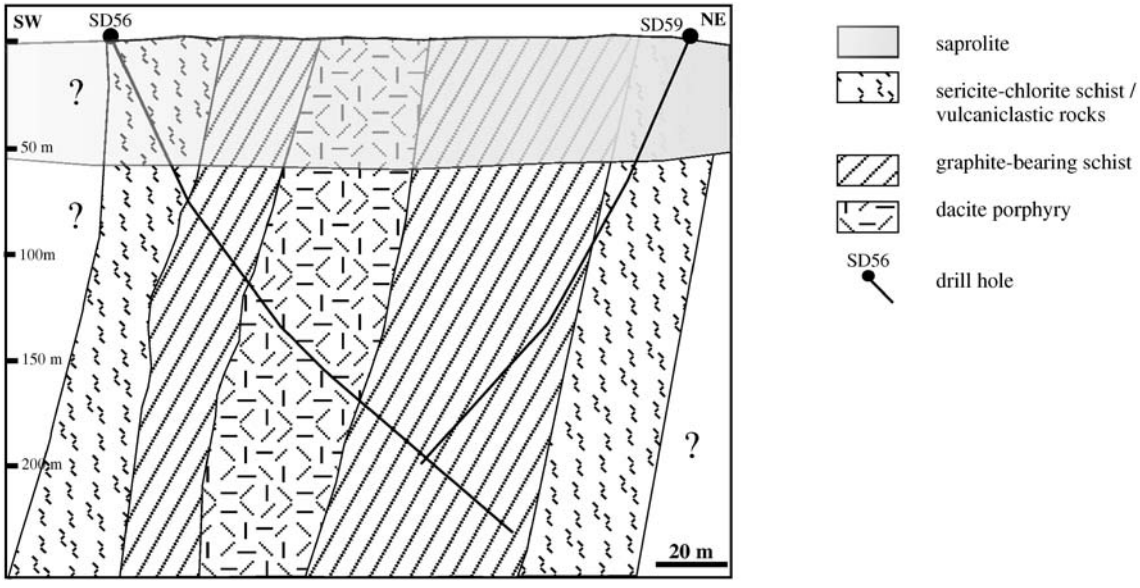

Fig. 3 Cross-section of the Serrinha deposit. Mineralized zones are restricted to the graphite-bearing layer crosscut by the drill holes

artisanal (*garimpo*) official production from 1965 to 1996 is of 15.5 tonnes Au for these two deposits (Araujo Neto 1998). More recently, Torresini (2000) reported resources of 60 tonnes Au grading 1.4 g/t Au for the Cipoeiro and Chega Tudo deposits, whereas the Cachoeira deposit produced about 1.2 tonne Au and holds geologic resources of calc. 20 tonnes Au (Klein et al. 2005a and references therein).

Geology and gold mineralization in the Serrinha deposit

Several open pits, worked by small miners that exposed mainly superficial and oxidized mineralization, and diamond drilling (four holes) down to 210 m revealed the main geologic features of the Serrinha gold deposit (Figs. 2 and 3). Below about 50 m of supergene cover, the stratigraphy of the deposit is comprised of graphitic schists in addition to subordinate volcanic and volcaniclastic rocks that belong to the Paleoproterozoic Chega Tudo Formation. These rocks occur as subvertical and subparallel layers (Fig. 3) showing a pervasive NW–SE trending schistosity that dips at high angles to the southwest and parallels the regional structural grain of the Gurupi Belt. Part of the schists outside the mineralized zones is composed of sericite and chlorite that occur in variable proportions with chlorite being the predominant mineral in some places. They contain abundant layers of volcaniclastic rocks and graphite-bearing schists and are crosscut by barren quartz veins. The graphitic schists are the most common rock type in the deposit, consisting of fine- to medium-grained dark-colored foliated rocks (Fig. 4a,b). The volcanic rock is a foliated dacite porphyry that occurs between layers of graphite-bearing schists. The dacite layer is weakly altered in narrow, centimeter-thick bands composed of carbonaceous matter (graphite?), quartz, carbonate, sericite, and sulfide minerals. As a whole, the volcano-sedimentary sequence underwent deformation under ductile–brittle conditions.

Mineralized zones at Serrinha are discontinuous and boudinaged both along strike and at depth, extending for at least 2 km in length and 210 m in depth. Two mineralized zones were intersected by drill hole SD56 (levels 175 and 206) with both zones being restricted to the graphitic schists that occur in the deepest part of the deposit (Fig. 3). These zones are up to 11-m-thick and mostly conformable to the schistosity. Within the ore zones, the hydrothermal alteration is characterized by silicification, carbonatization, and sulfidation and the mineralization style is very simple consisting of millimeter- to centimeter-thick quartz-carbonate veins, in addition to sulfides that occur both in the veins and as disseminations in the wall rock. The milky

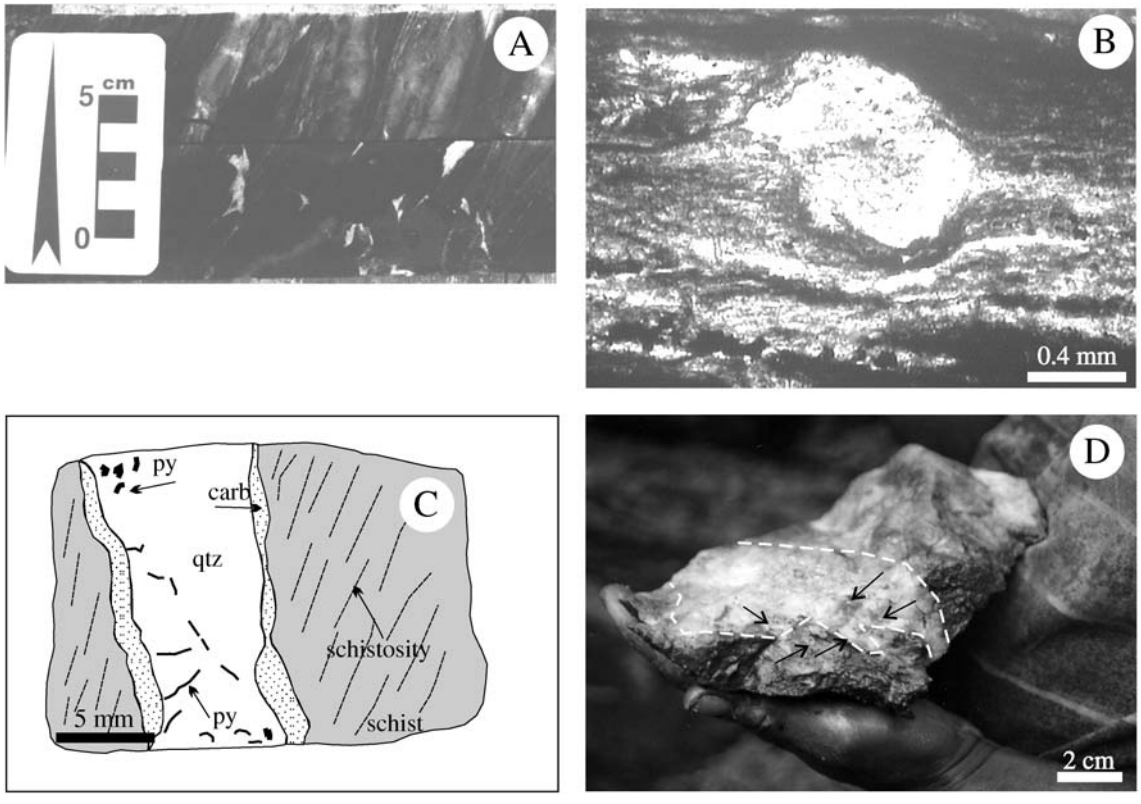

Fig. 4 **a** Polished slab of a graphite-bearing schist in the mineralized zone of the level 206 m, showing the foliation concordant quartz-carbonate veinlets (*top*), and irregular spots of quartz-carbonate (*bottom*). **b** Photomicrography of the sheared host schist showing a rotated quartz porphyroblast. *Dark areas* are graphite-rich and *white areas* are carbonate-rich. **c** Sketch showing relationships between the quartz (*qtz*)-carbonate (*carb*)- sulfide (*py*) veinlets, and the host schist. Note the distribution of carbonates in the *margins* of the veinlet. **d** Photograph of a gold-bearing quartz vein, outlined by *white dashed lines*, crosscutting a graphite-bearing schist (*light gray*), and showing free *gold particles* (*arrows*)

quartz-carbonate veinlets are also discontinuous in length and in general, they show sharp contacts with the host schists. Furthermore, these veinlets are parallel to slightly oblique in relation to the schistosity (Fig. 4a,c). This indicates that they filled openings in the foliation planes and that they are postmetamorphic. Some veinlets have a locally laminated appearance shown by thin slivers of the wall rock (Fig. 4a), suggesting that they developed within an active structure. Despite this character, the veinlets are less deformed than the immediate host rock (Fig. 4b), indicating their late timing with respect to the peak of the deformation. In places, quartz and carbonate form only centimeter-wide irregular spots, cutting across the schistosity (Fig. 4a), also indicating the postmetamorphic timing of their development. Thicker veins tend to be massive (Fig. 4d).

Most of the veinlets have quartz cores and carbonate margins. Textural relationships show evidence of distinct timing of quartz and carbonate precipitation in level 175 (upper level) and of coprecipitation in level 206 (lower level) (Fig. 5a,b). In addition, the composition of the carbonate phases also differs in the two levels, calcite and ankerite in the upper level and calcite and dolomite in the lower level. These carbonates are subhedral to euhedral and occur in proportions that vary between 10 and 50vol.% of the veinlets. In general, the calcite to ankerite ratio is 4:1

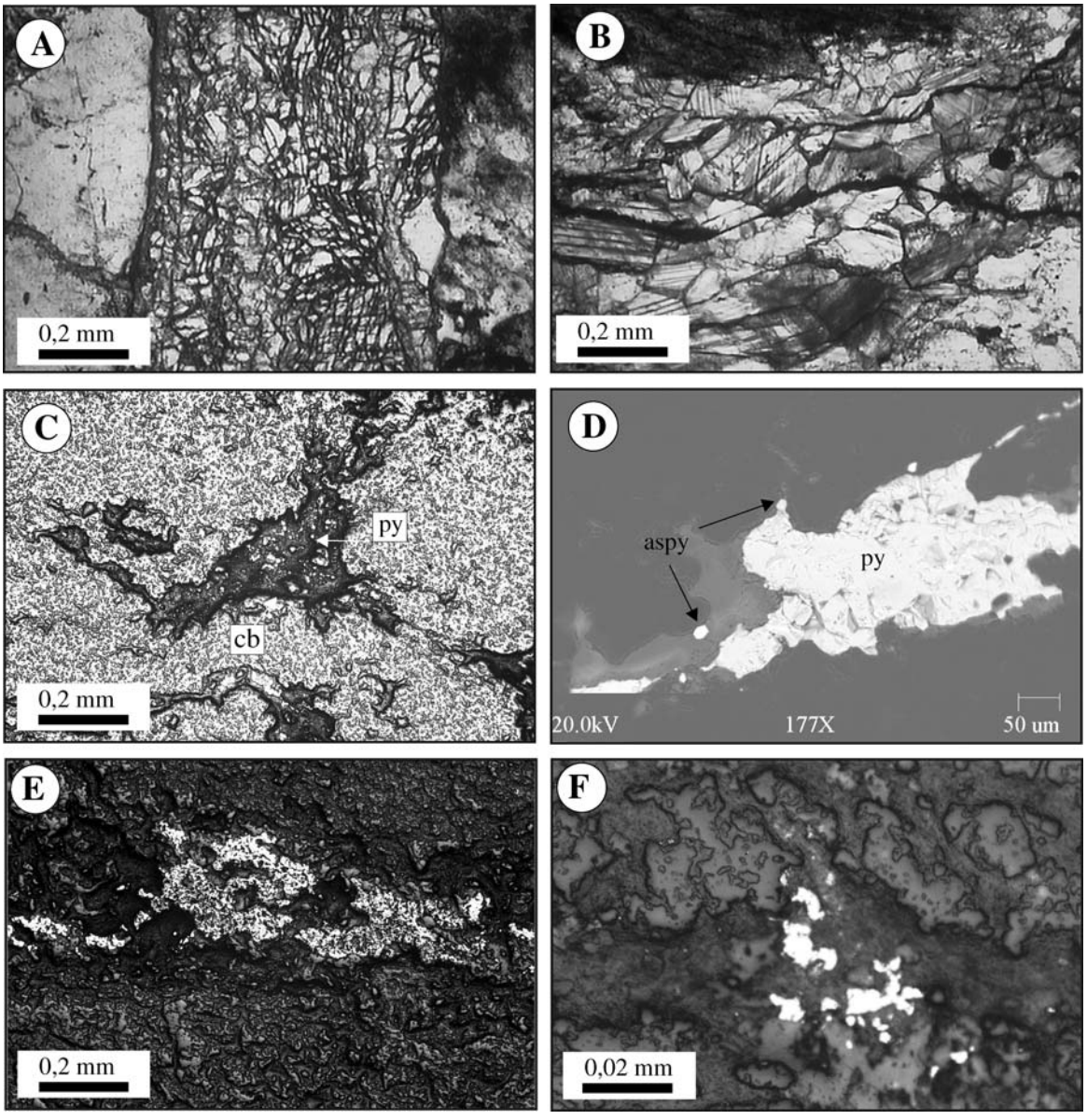

Fig. 5 Photomicrographs showing mineralogical and textural aspects of the hydrothermal alteration. **a** Veinlet of the level 175 m showing the sharp contact between quartz (*left*) and carbonate (*center*). **b** Veinlet of the level 206 m with evidence of coprecipitation of quartz and carbonate. **c** Dissemination of very fine-grained pyrite (*py*) in carbonate aggregate (*carb*) of the level 206 m. **d** Backscattered image of an irregular pyrite grain (*py*) with small crystals of arsenopyrite (*arrows*) located in a quartz-carbonate vein of level 206 m. **e** Elongated pyrrhotite within the foliation of a graphite-bearing schist out of the mineralized zones. **f** Irregular free *gold particles* in a quartz-carbonate vein of level 206 m

and calcite to dolomite ratio is 1:1. The vein quartz is generally fine-grained, anhedral, and does not show any preferred orientation or growth zones. It shows effects of deformation under variable intensities such as moderate to strong undulose extinction, a few deformation lamellae, and brittle fractures. Some larger crystals show subgrains developed at their boundaries due to dynamic recrystallization.

Pyrite is the dominant sulfide mineral. It occurs mostly as fine-grained subhedral to anhedral crystals filling microfractures in the quartz-carbonate veinlets (Figs. 4c and 5c) and subordinately as disseminations in the wall rocks. Arsenopyrite occurring as isolated grains near larger pyrite crystals (Fig. 5d) and galena occurring as spots over pyrite are very fine-grained and were detected only in SEM analysis. Pyrrhotite, arsenopyrite, and ilmenite occur outside the ore zones where pyrite is subordinate. Pyrrhotite is always anhedral and coarse-grained, occurring generally as discontinuous submillimetric layers or elongated crystal aggregates within the foliation planes in association with carbonates (Fig. 5e). Arsenopyrite is, in general, fine-grained and in places, it shows pyrite overgrowths in small fractures. Ilmenite and pyrite are very fine-grained.

Gold occurs both in the upper and lower ore zones at a grade of 0.5 to 1.3 ppm Au. Most of the gold occurs in the free state, forming aggregates in fractures and interstitial grain pores in the quartz-carbonate veins and in the vein-wall rock contacts. The gold particles are generally undeformed and irregularly shaped (Fig. 5f) having submicroscopic sizes but are also visible (Fig. 4d). These textural relationships indicate that gold formed late in the deformational evolution but also during fluid–wall rock reactions. In addition, subordinate gold was also detected as a trace element (~0.6wt%) by semiquantitative scanning electron microscope and energy dispersive spectrometer analysis of pyrite crystals from quartz-carbonate veinlets and from the wall rock.

Analytical procedures

Fluid inclusion studies were carried out on quartz from narrow quartz-carbonate veinlets representative of the upper and lower mineralized zones. Sample preparation and analysis followed procedures described in Shepherd et al. (1985) and Roedder (1984). After petrographic evaluation, the microthermometric analysis was performed with a Chaixmeca heating–freezing stage at the Universidade Federal do Pará, in Belém, Brazil. Calibration was done with synthetic standards including pure CO_2 (−56.6°C) and water (0.0°C). Precision was estimated to be ±0.3°C for runs below 30°C and ±5°C for runs above 100°C. Raman microspectroscopic analysis was carried out at the Universidade Federal de Minas Gerais, in Belo Horizonte, Brazil, using a multichannel Dilor XY spectrometer. The exciting source was an argon laser with a wavelength of 514.53 nm and an output of 700 mW laser power at the source. Integration time was 10 s with ten accumulations for each spectral line. Molar proportions were calculated using the relative Raman scattering cross-sections of 2.5 for CO_2, 7.5 for CH_4, and 1.0 for N_2 as suggested by Burke (2001).

Carbon, oxygen, and hydrogen isotope analyses were performed with a Micromass-Isoprime, gas-source mass spectrometer at the Laboratoire des Isotopes Stables of the Université Jean Monnet, Saint Etienne, France. Sulfur isotopes were analyzed with a Finnigan MAT 252 mass spectrometer at the Stable Isotope and ICP/MS laboratory of the Queen's University, Kingston, Canada. All mineral separates were estimated to be >95% pure. For carbonate minerals, 5–10 mg of dry powder were analyzed. The samples were reacted overnight in vacuum with 2 ml of 100% H_3PO_4 to produce CO_2. Calcite was reacted at 25°C (McRea 1950), whereas ankerite and dolomite were reacted at 50°C (Al-Assam et al. 1990). The extracted CO_2 was cryogenically purified. Analysis of duplicates produced results that agree within 0.2‰ for both $\delta^{13}C$ and $\delta^{18}O$. Data were corrected using the carbonate-phosphoric acid fractionation factors of 1.01025 for calcite (Friedman and O'Neil 1977), 1.01065 for dolomite, and 1.01057 for ankerite (Rosenbaum and Sheppard 1986). For oxygen isotope analysis of quartz, a laser fluorination system (Harris et al. 2000) was used. Oxygen was produced by heating grains weighing typically 2 to 4 mg with a 40-W CO_2 laser in an atmosphere of BrF_5, which was then converted to CO_2 by reaction with graphite, and was cryogenically purified. An internal standard (MONGT, $\delta^{18}O$=+5.55‰) was analyzed to calibrate the data to the standard mean ocean water (SMOW) scale. Rapid heating using a defocused beam (Spicuzza et al. 1998) was used to minimize sample loss of material during the reaction and yields were on average 92% of the expected amount for quartz. The missing material in all cases appeared to be ejected during the initial heating before reaction with the BrF_5. Although duplicate analyses of three selected samples gave agreement within 0.2‰, multiple analyses of two samples analyzed during the course of this work gave a spread of 1.2 and 0.6‰ (n=4). This variation in $\delta^{18}O$ must however be due to a combination of analytical precision and oxygen isotope inhomogeneity in the sample. Inclusion fluids (H_2O, CO_2) were extracted from ~2 g of degassed quartz (70–200°C) by thermal decrepitation in an evacuated quartz tube inductively heated at >800°C. Water was purified cryogenically and then reduced to H_2 by reaction with "Indiana Zn" at 450°C, according to procedures adapted from Coleman et al. (1982), and precision is estimated at ±4‰. Any CO_2 present was removed cryogenically and the carbon isotope composition was determined. Graphite was also analyzed for its carbon isotope composition using the standard off-line reduction method. For sulfur analysis, SO_2 was produced from 3 to 10 mg of sulfide minerals loaded into tin capsules and reacted with CuO at 1,400°C in a He stream using the thermal conversion/elemental analyzer-isotope ratio mass spectrometer technique. The analytical uncertainty for $\delta^{34}S$ is 0.5‰. All data are reported in the delta notation relative

to PeeDee Belemnite (C), SMOW (O and H), and Canyon Diablo Triolite (S).

Fluid inclusions

Fluid inclusion studies were performed on the larger and better preserved quartz grains of quartz-carbonate veinlets from the upper (level 175) and lower (level 206) mineralized zones. Recrystallized grains or grains suspected of having been recrystallized were avoided in the microthermometric work. About 170 inclusions were investigated and no workable fluid inclusions were found in the carbonate crystals. The following abbreviations concerning the temperatures of phase changes are used in the text, tables, and figures:

$TmCO_2$:	final melting of the solid CO_2
Tmclat:	melting of clathrates
$ThCO_2$:	(partial) homogenization of CO_2
Tht:	final homogenization (L: into liquid and V: into vapor)
VCO_2:	volume of the carbonic phase (vol.% CO_2/vol. total in %)

Petrography, distribution, and types

The fluid inclusions are small (<10 μm) and mostly distributed in the inner portions of the quartz grains along intragranular three-dimensional planar arrays (Fig. 6) that are both perpendicular and parallel to the vein walls. Some inclusions also show random three-dimensional distribution (Fig. 6) occurring in isolation, in discrete clusters, or in short trails in the inner portions of the quartz. The trail-bound and the randomly distributed fluid inclusions show dominantly negative crystal shapes (Fig. 6). These inclusions are not considered primary but they trapped early fluids that percolated during the evolution of the gold-bearing veinlets and of the hydrothermal system. These early inclusions are CO_2-bearing and two types were distinguished on the basis of phase proportions at room temperature and behavior under freezing–heating. Type 1 comprises one- and two-phase carbonic inclusions. They are generally dark with no visible water at room temperature and occur in close association with the type 2 inclusions. Type 2 is composed of two-phase (sometimes three-phase) aqueous-carbonic inclusions. These type 2 inclusions have the gaseous (carbonic) phase occupying between 30 and 80% (mostly 40–60%) of the total inclusion volume (Fig. 6). A third type comprises aqueous inclusions. These are rare and restricted to the upper level of the mine where they occur in sharp trails that cut across the two other types, that is, they are texturally late secondary inclusions.

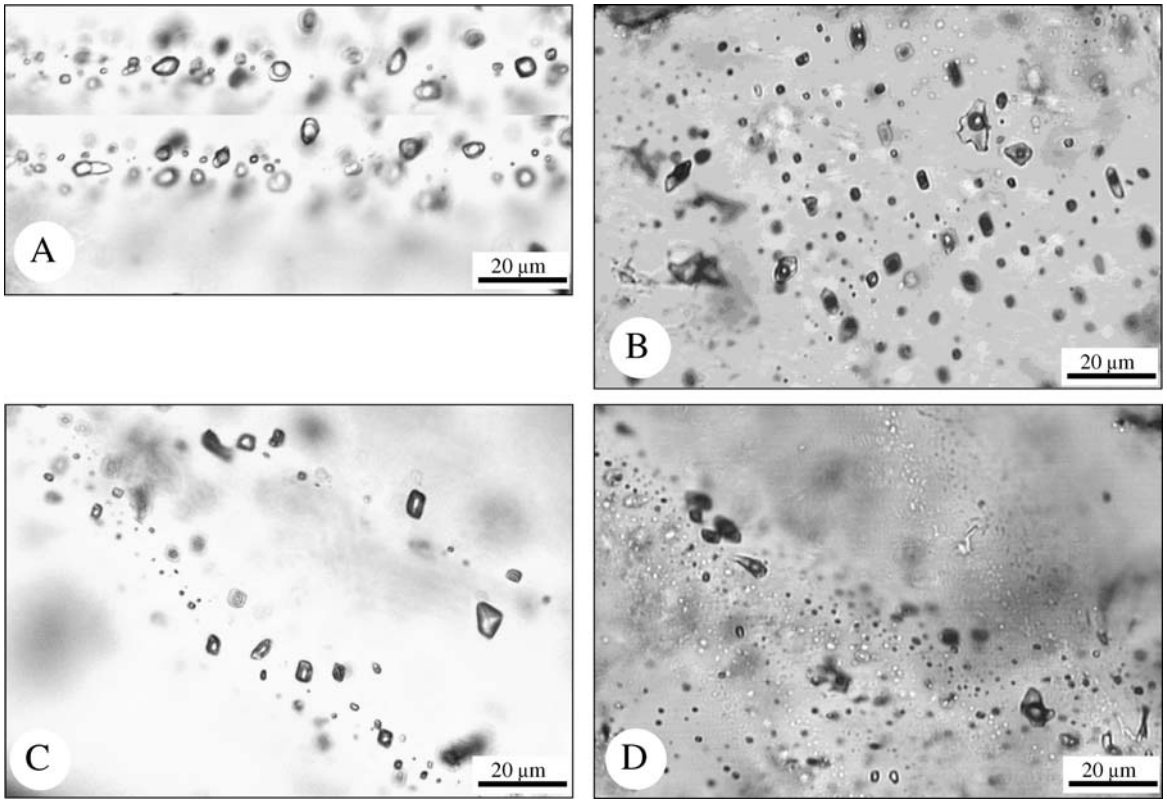

Fig. 6 Photomicrographs showing the distribution of carbonic and aqueous-carbonic fluid inclusions in the upper (**a** and **b**) and lower (**c** and **d**) mineralized zones. Note the very variable CO_2/H_2O proportions in a single microscopic domain in both *upper* and *lower zones*

Microthermometry and laser Raman data

The microthermometric results show that the carbonic phase in both carbonic and aqueous-carbonic fluid inclusions melted between −59.9 and −56.8°C with most of the values clustering tightly within the −58.0 to −57.5°C interval (Fig. 7). The distribution of temperature values is similar in the two levels but values lower than −58.5°C are restricted to the lower level (Figs. 7 and 8). Raman analyses of selected inclusions (Table 1) revealed that the carbonic phase is composed chiefly of CO_2 (91 to ~100mol%) along with minor amounts of N_2 (2–9mol%) and CH_4 (up to 2mol%).

The homogenization of the carbonic phase to liquid covers a wide temperature range from −11.8 to 28.1°C in level 206 and a more restricted range from 11.5° to 29°C in level 175 (Fig. 7), implying very variable CO_2 and bulk densities. Type 2 inclusions show identical CO_2(L) temperature distribution in the two levels with all values being higher than 8°C. Conversely, all temperatures lower than 8°C are restricted to type 1 inclusions of level 206. The overall frequency distribution is multimodal with peaks at 9, 17, and 23°C and asymmetric with the histogram skewed to the right (Fig. 7). Variations in excess of 15°C are found at the scale of a single microscopic domain (Fig. 8a) and there is no clear relationship between $ThCO_2$ and the composition ($TmCO_2$) of the nonaqueous phase (Fig. 8c).

The final dissolution of the clathrates in type 2 fluid inclusions occurred always before the partial homogenization of the carbonic phase. The overwhelming majority of the inclusions have Tmclat between 6.8 and 9°C with >80% of the values clustering at 7 to 8°C (Fig. 7). This defines a salinity of 4.5wt% NaCl equiv. Eight, out of 89 investigated fluid inclusions have Tmclat between −1.7 and −0.7°C, implying higher salinities (19–21wt% NaCl equiv). One inclusion showed the dissolution of clathrate at 12.5°C, which can be attributed to the presence of CH_4 (Collins 1979).

The final homogenization occurred also in a wide range of temperatures between 250 and 430°C, both to the liquid and to the gaseous phase (Figs. 7d and 9). A mode for the whole set of investigated inclusions is observed at 310°C and most of the values are in the 280 to 340°C range (average of 332±41°C). It is noteworthy to point out the pronounced skewness of the frequency histogram with the mode close to the lower homogenization temperature region (Fig. 7; see interpretation below).

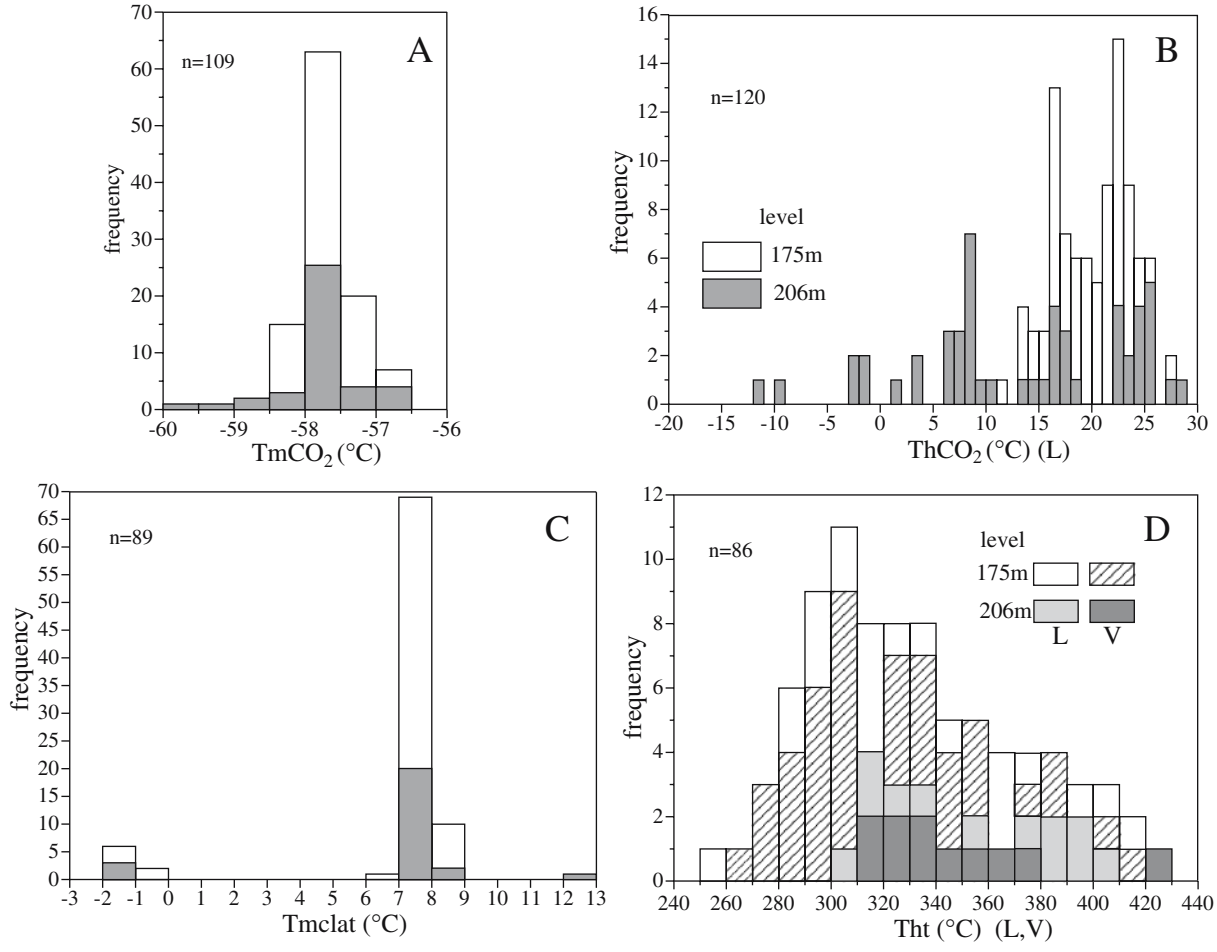

Fig. 7 Frequency histograms showing the distribution of the microthermometric properties of the fluid inclusions. **a** Melting of the carbonic phase. **b** Homogenization of the carbonic phase. **c** Dissolution of clathrates. **d** Final homogenization into liquid and vapor

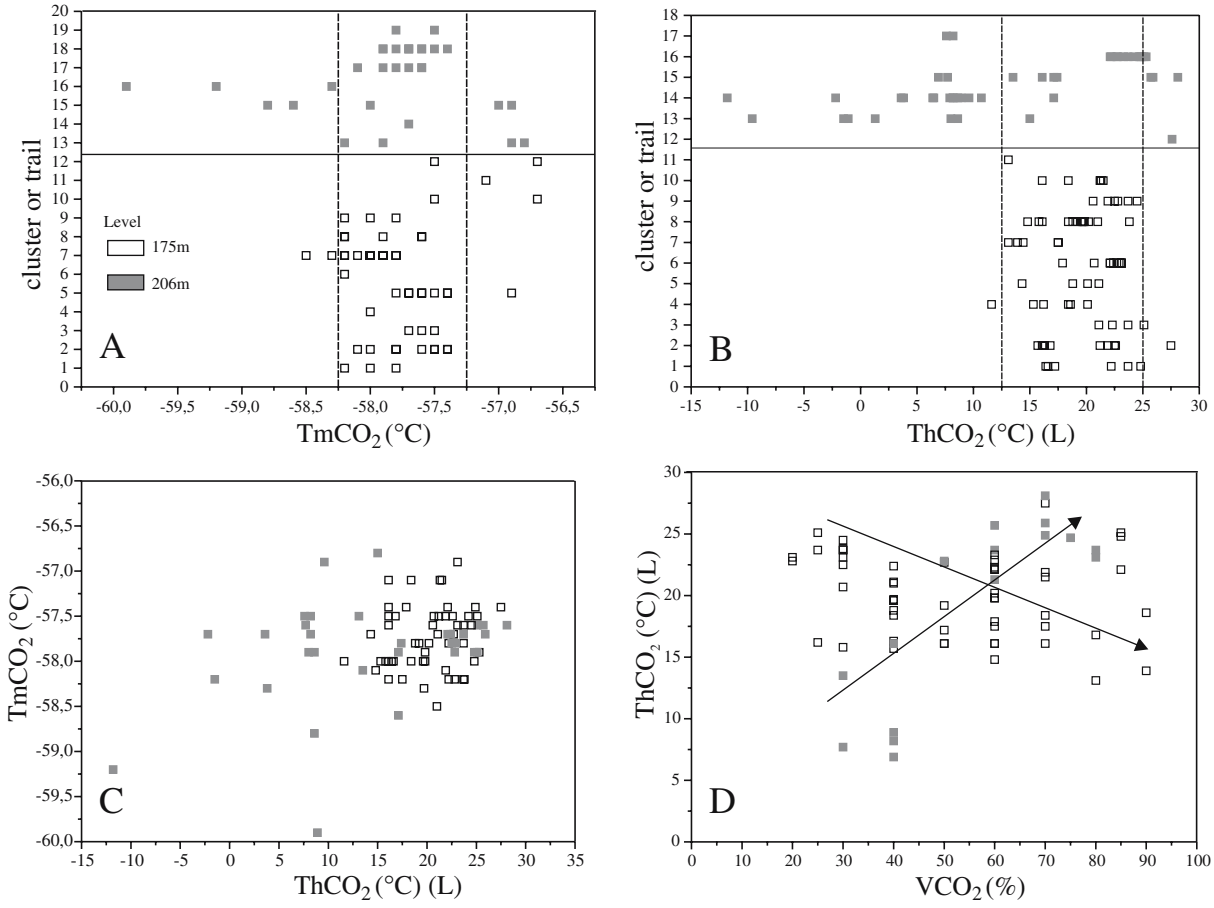

Fig. 8 Diagrams showing relationships between fluid inclusion properties. **a** Distribution of homogenization of the carbonic phase and **b** melting of the carbonic phase. Each *horizontal field* represents a single cluster or trail. **c** Diagram showing absence of correlation between $ThCO_2$ and $TmCO_2$. **d** $ThCO_2$ vs volume of the carbonic phase diagram. The *arrows* show possible trends. All *symbols* are as in diagram **a**

The studied samples lack primary or pseudosecondary aqueous inclusions in equilibrium with type 1 and 2 inclusions. Only a few texturally late inclusions were documented in the upper level. These inclusions homogenized between 176 and 205°C into liquid, confirming their late timing with respect to the carbonic inclusions.

Interpretation of fluid inclusion data

Fluid inclusion populations

Fonarev et al. (1998) proposed the concept of group of synchronous inclusions (GSI), which is basically a fluid inclusion assemblage (FIA) in the sense of Goldstein and

Table 1 Composition of the carbonic phase of selected carbonic (type 1) and aqueous carbonic (type 2) fluid inclusions of the Serrinha gold deposit estimated from combined microthermometric and Raman spectroscopic analyses

Sample/fluid inclusion	Type	VCO_2 (%)	$TmCO_2$ (°C)	$ThCO_2$ (°C)	Tmclat (°C)	Tht (°C)	CO_2(%)	CH_4(%)	N_2(%)
Upper level									
175/3–5	1	100	−58.8	14.4	–	–	94	2	4
175/3–1	2	70	−58.2	17.5	7.8	347	91	tr[a]	9
175/3–8	2	60	−58.0	19.8	7.8	359	91	1	2
Lower level									
206/4–1	1	100	−58.3	3.8	–	–	97	tr	3
206/4–2	2	40	−59.9	8.9	8.5	>241[b]	93	tr	7
206/6–1	2	70	−57.7	24.9	7.3	314	100	nd[c]	nd

[a]Traces
[b]Decrepitation temperature
[c]Not detected

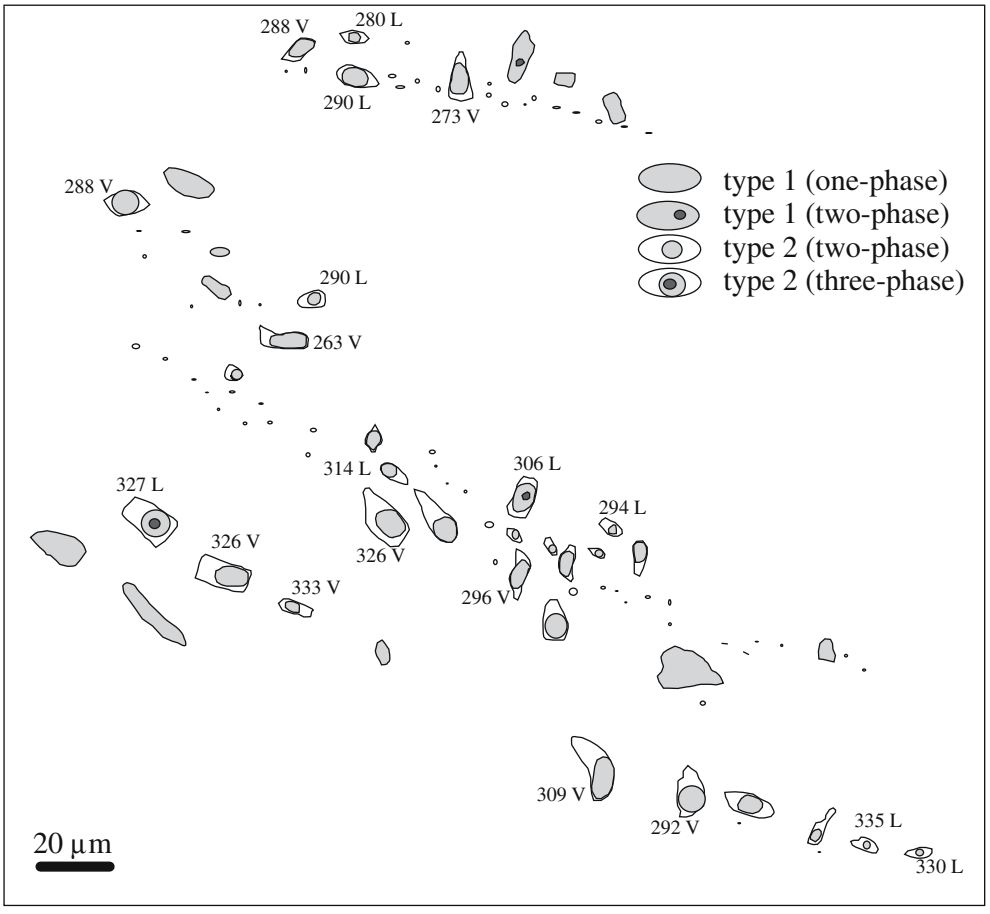

Fig. 9 Hand drawn sketch showing the distribution and textural relationships between the different types of CO_2-bearing fluid inclusions. The *numbers* beside the inclusions indicate the final homogenization temperature (*L* to liquid and *V* to vapor)

Reynolds (1994). A GSI/FIA represents a group (a trail or a cluster) of related inclusions contained in a single crystal or occurring in a single domain of a crystal within the field of view of the microscope. Such a group consists of coeval and cogenetic inclusions that trapped the same fluid. Accordingly, microthermometric results of each GSI should be plotted separately and compared in diagrams of CO_2 homogenization and melting temperatures.

Using this approach to the fluid inclusions of the Serrinha deposit (Fig. 8a,b), two behaviors can be observed. First, regardless of the mineralized level, most of the inclusions plot in a same field of $ThCO_2$ and $TmCO_2$, indicating that they trapped the same fluid. These are the dominant aqueous-carbonic (type 2) fluid inclusions. Second, fewer inclusions plot in a distinct field, having lower $TmCO_2$ and especially lower $ThCO_2$ (higher density). These inclusions are restricted to the lower mineralized level and are mostly CO_2-rich (type 1), subordinately aqueous-carbonic (type 2) inclusions, and both contain subordinate amounts of $N_2 \pm CH_4$.

Composition and density

Bulk compositions, density, and isochores (Fig. 10) were calculated from microthermometric and Raman data using the Flincor program (Brown 1989) and the equation of Bowers and Helgeson (1983) for the aqueous-carbonic inclusions, which represent best the ore-bearing fluid. The bulk composition of the fluid is XCO_2: 8–75mol% (typically 18–33mol%); XH_2O: 24–91mol% (typically 66–80mol%); XN_2: <4mol%; XCH_4: <<2mol%; and XNaCl: 1–2mol%. CO_2 densities vary from 0.66 to 0.88 g/cm^3, chiefly 0.81–0.87 g/cm^3; bulk densities are in the range of 0.75 to 0.98 g/cm^3, mainly 0.89–0.94 g/cm^3; and salinity is 4.5wt% NaCl equiv.

The role of CH_4 and N_2

It is known (Collins 1979; Seitz and Pasteris 1990; Diamond 1994; Hagemann and Brown 1996; Van den Kerkhof and Thiéry 2001) that the presence of CH_4 and/or N_2 in the CO_2-H_2O-salt system may affect some microthermometric properties and can cause misestimation of fluid salinity, density, and trapping pressures. At Serrinha, these volatiles are subordinate but a general relationship between the amount of $CH_4 + N_2$ and the melting and partial homogenization of the carbonic phase is observed in that higher contents of these compounds are associated with lower CO_2 melting and homogenization temperatures (Table 1). These variations are well constrained and they may also explain the entire range in density variations. The consistency of the salinity data precludes significant influence of the CH_4 and N_2 contents, except for a single Tmclat value of 12.5°C that is likely related to the presence

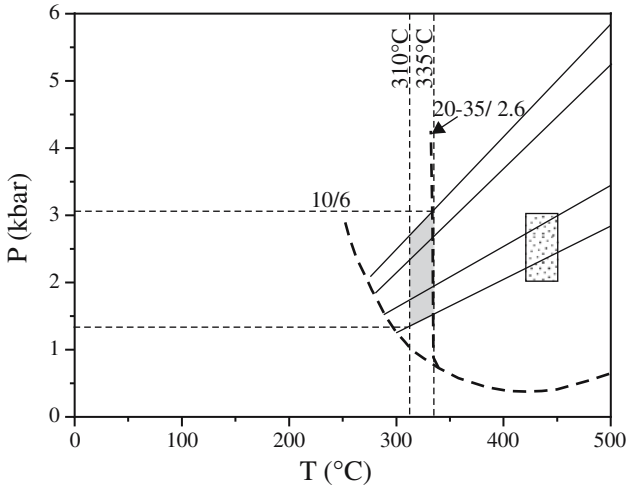

Fig. 10 P-T diagram showing the estimated conditions for gold mineralization at Serrinha (*shaded box*). The *stippled box* limits the conditions of the metamorphic peak (data from Yamaguti and Villas 2003) of the hosting metavolcano-sedimentary sequence. The *thick dashed lines* are solvi for the CO_2-H_2O-NaCl system. *Numbers* near the solvi indicate mol% CO_2 and wt% NaCl equiv. The solvi labeled 10/6 and 20-35/2.6 are from Bowers and Helgeson (1983) and Hendel and Hollister (1981), respectively

of CH_4. As such, the salinities determined from the largely predominant group of inclusions are considered as good estimations for the composition of the ore-forming fluid at Serrinha.

Regarding the source of CH_4 and N_2, contamination of CO_2-bearing fluids by reaction with rocks containing organic matter is widely invoked to explain the presence of CH_4 and N_2 in fluid inclusions from shear zone-hosted gold deposits, based on the commonly observed presence of carbonaceous rocks, either hosting gold mineralization or in the ore environment (e.g., Naden and Shepherd 1989; Shepherd et al. 1991). This may occur either in the ascent of the fluid through the metavolcano-sedimentary sequence or near the site of deposition. On the other hand, during the continuous phase separation of a CO_2-CH_4-N_2-H_2O-NaCl fluid, the CH_4 and N_2 proportions tend to diminish toward the end of the process because methane and N_2 have higher volatilities or gas distribution coefficients than CO_2 (Henley et al. 1984; Drummond and Ohmoto 1985; Naden and Shepherd 1989). Accordingly, immiscibility could also explain the observed variations in the relative proportions of CO_2, CH_4, and N_2 in the fluid. Nevertheless, as will be shown below in the "Stable isotopes" section, at least part of the carbon present in the fluid inclusion CO_2 may be derived from the host rocks.

Fluid immiscibility and postentrapment modification

The petrographic and microthermometric characteristics of the fluid inclusions from quartz samples of the Serrinha deposit, namely, wide variation in the phase ratios, temperature of homogenization of the carbonic phase (density variation), and in the final homogenization temperatures into liquid and vapor of coexisting inclusions, are typical of the heterogeneous state. This may be produced either by entrapment of immiscible fluids (mechanical mixture of two end members; Anderson et al. 1992) or of an initially homogeneous fluid undergoing effervescence (Loucks 2000; Diamond 2001; Van den Kerkhof and Hein 2001). The absence of coeval and spatially related aqueous inclusions and the correlation between final homogenization temperatures and salinity (Cathelineau and Marignac 1994; Dugdale and Hagemann 2001) preclude mixing. In addition, in the type 2 aqueous-carbonic inclusions, total homogenization temperature occurs in the same temperature range, both to the liquid and to the gaseous phase (Figs. 7d and 9), satisfying another criterion for fluid immiscibility (Ramboz et al. 1982; Diamond 2001). Furthermore, the asymmetric frequency distribution of the partial and total homogenization temperatures (Fig. 7b,d) is also compatible with immiscibility (Loucks 2000; Diamond 2001; Touret 2001).

The heterogeneous state and the observed variations might also be produced by postentrapment modifications (Crawford and Hollister 1986; Huizenga and Touret 1999; Loucks 2000). Inclusions clearly showing textures of postentrapment modification, such as necking down, decrepitation clusters, and microfractures, were avoided in the microthermometric work. Nevertheless, there is microstructural evidence of recrystallization and grain boundary migration of the host quartz and the analysis of the microthermometric data indicates that postentrapment changes could have occurred. The following points must be considered:

1) The correlation between $ThCO_2$ (i.e., density) and the phase ratios. According to Huizenga and Touret (1999), aqueous-carbonic inclusions in which selective water leakage occurred should have water-rich inclusions (lower VCO_2) with densities higher (or lower $ThCO_2$) than the densities of the water-poor inclusions (higher VCO_2). This is possible for level 206 but not for level 175 (Fig. 8d) where the opposite trend that indicates phase separation is roughly shown. Because strain distribution within an evolving structure or even within a single vein is usually heterogeneous (Sibson 1990), and given the microstructural evidence that quartz from the veinlets at Serrinha was variably affected by deformation, some selective water removal might have occurred in the lower zone.
2) The highest densities are concentrated in type 1 fluid inclusions. These inclusions were not produced by H_2O leakage because this would lead to a density decrease in the remaining fluid.
3) The multimodal distribution of the homogenization of the carbonic phase (Fig. 7b). This may reflect a P-T path after inclusion formation that arises from reequilibration of fluid inclusions due to fluctuations in the trapping pressure, necking down, or leakage (Wilkins and Barkas 1978; Dubessy 1994; Vityk and Bodnar 1995; Huizenga and Touret 1999). Isochores calculated using the lowest and highest densities of the

aqueous-carbonic fluid inclusions (Fig. 10) show a wide range of trapping pressures for a given temperature. According to Robert et al. (1995), despite the fact that such pressure values must be considered with caution, this pressure range is too large (about 2 kbar for 310°C in level 206) to be accounted for only by postentrapment modifications and implies significant pressure variations during vein development. Furthermore, as shown in Fig. 8b, $ThCO_2$ (i.e., density) variations of more than 15°C were documented in many individual clusters or trails of synchronous inclusions. This is more likely produced by pressure variations.

4) In the few type 2 inclusions with clathrate melting at negative temperatures (i.e., having the highest salinities), there is no unequivocal explanation for their occurrence. The addition of large amounts (>15mol%) of N_2 to CO_2 lowers the temperature of clathrate dissociation (Diamond 1994). However, the amount of N_2 at Serrinha is small and the temperature of melting of the carbonic phase in these high-salinity inclusions does not differ from those of the dominant low-salinity group. A raise in the salinity may also occur through selective postentrapment removal of water by a diffusion mechanism (Hall et al. 1991; Frantz et al. 1992) and during phase immiscibility, when salt partitions into the H_2O-rich phase (Ramboz et al. 1982). However, these higher salinities occur in both CO_2- and H_2O-rich inclusions (VCO_2 30–90%). In addition to the higher salinity, these few inclusions occur in isolation without any spatial relationship with the major group of type 2 fluid inclusions and they all homogenize above 366°C, both to liquid and vapor. Because mixing was discarded, they may represent relics of an earlier, hotter, and more saline fluid or inclusions in which water leakage occurred via diffusion. The latter hypothesis seems to be more probable.

5) The absence of primary or pseudosecondary aqueous inclusions in equilibrium with type 1 and 2 inclusions, which is not common in cases of fluid immiscibility. A possible explanation for this fact could be the occurrence of unmixing before the trapping of the inclusions. As such, the density and wetting contrasts between CO_2 and H_2O would favor trapping CO_2-rich inclusions and the removal of H_2O along microcracks and grain boundaries (Crawford and Hollister 1986). Even in this case, the trapping of some water either as mixed CO_2-dominated aqueous-carbonic inclusions or as pure aqueous inclusions along grain boundaries or fractures should be expected (Crawford and Hollister 1986). However, the predominance of mixed CO_2-H_2O (type 2) inclusions, having variable VCO_2, from H_2O-rich to CO_2-rich inclusions indicates that CO_2 and H_2O were not physically isolated from each other. This is also reinforced by the fact that water is necessary to the transport of silica and gold complexes, which will eventually form gold-bearing quartz veins.

In summary, several criteria show conflicting evidence for fluid immiscibility and postentrapment modification in the same sample and both processes fail to explain alone the observed fluid inclusion characteristics. Therefore, we interpret the fluid inclusions of the Serrinha deposit to reflect the trapping of an effervescing (immiscible) aqueous-carbonic fluid under fluctuating pressure conditions, followed and/or accompanied by postentrapment modification produced by the plastic deformation of the host quartz. In case of immiscibility, any proportions of the end members can be trapped and it is possible that little or no water was trapped as pure aqueous inclusions. Although uncertain, the combination of fluid immiscibility and posttrapping selective removal of water could account for the absence of aqueous inclusions in equilibrium with carbonic and aqueous-carbonic inclusions.

Table 2 Measured isotopic compositions of hydrothermal minerals, inclusion fluids, and graphite

Sample/level	Mineral	Silicate	Carbonate/graphite		Fluid Inclusions		Pyrite
		$\delta^{18}O$ (‰)	$\delta^{13}C$ (‰)	$\delta^{18}O$ (‰)	$\delta^{13}C$ (‰)	δD (‰)	$\delta^{34}S$ (‰)
Upper level							
175	Quartz	+13.7			nd	−21	
175	Calcite		−14.2	+19.2			
175	Ankerite		−14.3	+17.5			
175	Graphite		−23.5				
175	Pyrite						−2.6
176	Quartz	+12.1			nd	−19	
Lower level							
206	Quartz	+13.4			−17.6	−80	
206	Calcite		−15.7	+12.3			
206	Dolomite		−15.0	+13.8			
206	Graphite		−23.6				
206	Pyrite						−7.9

nd Not detected

Stable isotopes

A reconnaissance stable isotope study was conduced on hydrothermal quartz, carbonates, and pyrite as well as in graphite samples from the host rock. The results are presented in Table 2. The $\delta^{13}C$ value of the graphite carbon is −23.5 and −23.6‰, in the upper (level 175) and lower (level 206) zones, respectively. Among the carbonate minerals, the $\delta^{13}C$ values of calcite and ankerite in the upper zone are nearly identical (−14.2 and −14.3‰), respectively, whereas the $\delta^{18}O$ value is +19.2‰ in calcite and +17.5‰ in ankerite. In the lower zone, the $\delta^{13}C$ values of calcite and dolomite are also similar, being −15.7 and −15.0‰, respectively, and the $\delta^{18}O$ values are +12.3‰ in calcite and +13.8‰ in dolomite. The similar $\delta^{13}C$ values of distinct carbonate phases within individual veinlets are expected due to the small magnitude of carbon isotope fractionation between coexisting carbonates under hydrothermal conditions (e.g., Kyser 1987). On the other hand, the oxygen isotope ratios of the carbonates are significantly different in the two mineralized levels and could indicate some isotopic disequilibrium, reequilibration with fluids over time, not affecting the carbon isotopes or deposition from different fluids. The quartz of the quartz-carbonate veinlets shows $\delta^{18}O$ values of +13.7 and +12.7‰ in the upper zone and +13.4‰ in the lower zone. These nearly identical values suggest that quartz precipitated from the same fluid and at the same temperature in the two distinct levels. However, the quartz is only in oxygen isotope equilibrium with the carbonates of the lower level, which agrees with the petrographic evidence. Water extracted from fluid inclusions gave δD values of −21 and −19‰ in the upper level and a sample from the lower level gave a δD value of −80‰. A CO_2 fraction was also recovered from this sample of the lower level giving a $\delta^{13}C$ value of −17.6‰ for the CO_2 carbon. Sulfur from pyrite has $\delta^{34}S$ values of −2.6 and −7.9‰ in the upper and lower zones, respectively.

P–T–fO_2

Accepting phase separation as the most probable process that produced the fluid inclusions characteristics as seen at Serrinha, it is more likely that the whole range of fluid inclusion homogenization temperatures reflects variations in the trapping pressures instead of temperature variations of ~100°C in a single vein. In addition, because the fluid inclusions were trapped on or near the solvus of the system, the homogenization temperatures need no pressure correction. In consequence, the modal value of 310°C is taken as a good approximation for the dominant trapping conditions at Serrinha. Equilibrium temperatures calculated from the oxygen isotope fractionation between the quartz–calcite pair of the lower level using the calibrations of Chiba et al. (1989) and Zheng (1999) are 315 and 335°C, respectively. In addition, the dolomite–calcite pair of the lower level returns a carbon isotope equilibrium temperature of 310°C according to the equation of Sheppard and Schwarcz (1970). All these results are in good agreement with the fluid inclusion homogenization temperatures data. Therefore, the range of 310 to 335°C is suggested as the more likely temperature interval for ore deposition at Serrinha.

Isochores were calculated for the full range of densities and XCO_2 (Fig. 10). Trapping pressures estimated by the combination of the isochores with the temperature range of 310 to 335°C are in the range of 1.3 to 3.0 kbar (Fig. 10). This is consistent with the structural information, which indicates brittle–ductile behavior and mesozonal depths (8–10 km) for the development of the ore-hosting structure. Figure 10 also shows that these estimated conditions are consistent with a range of $XCO_2$and salinity values represented by two solvi of the CO_2-H_2O-NaCl system. Furthermore, a considerable part of the isochores passes through the field of the metamorphic peak conditions estimated by Yamaguti and Villas (2003) for the host metavolcano-sedimentary sequence.

Oxygen fugacities were calculated for the full range of XCO_2 at the assumed T–P range by applying the equations and equilibrium constant of Ohmoto and Kerrick (1977) and the fugacity coefficient of Ryzhenko and Volkov (1971). The obtained values for log fO_2 vary between −31.0 and −28.5. These values fall between the pyrite + magnetite/pyrrhotite and hematite/magnetite buffers above the CO_2-CH_4 buffer and below the SO_2/H_2S buffer (Fig. 11), indicating relatively reduced conditions for the ore-fluid. However, fO_2 was potentially more variable, possibly due to pressure variations as attested by the localized presence of pyrrhotite. Also, the immiscible separation of CO_2 trapped in the fluid inclusions and consumption of CO_2 to form the carbonates lead to the progressive oxidation of the fluid.

Fluid isotope composition and potential sources

The isotope composition of the hydrothermal fluid was calculated from mineral analysis at the temperature range

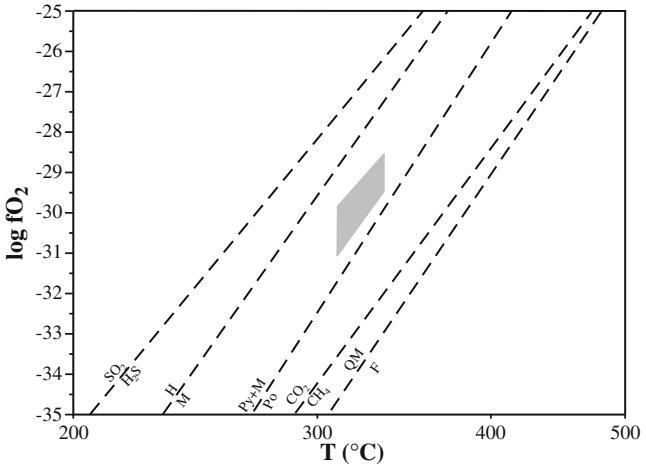

Fig. 11 T-fO_2 diagram showing the estimated redox conditions of the mineralizing fluid at Serrinha in relation to several solid and liquid buffers (references in Ohmoto and Goldhaber 1997)

of 310 to 335°C, using the appropriate fractionation factors. A summary of the calculated values is presented in Table 3. The oxygen isotope composition of the fluid in equilibrium with quartz was calculated by applying the quartz–water fractionation factor of Matsuhisa et al. (1979). The calculated $\delta^{18}O$ values of H_2O in the fluid vary between +6.2 and +8.0‰, being nearly identical in the two levels. The $\delta^{18}O_{H2O}$ values of the fluid in equilibrium with calcite and dolomite were calculated from the equations of Friedman and O'Neil (1977). In the lower level, the obtained values for $\delta^{18}O_{H2O}$ are in the range of +7.0 to +8.4‰ and are similar to those presented by the fluid in equilibrium with quartz. However, in the upper level the $\delta^{18}O_{H2O}$, values are very different, varying from +13.9 to +14.6‰. This reinforces the described petrographic equilibrium for the lower level and the disequilibrium in the upper level. These calculated $\delta^{18}O_{H2O}$ equilibrium values are compatible with both magmatic and metamorphic sources.

The hydrogen isotope composition of the fluid is taken from the measured δD_{H2O} value of aqueous-carbonic fluid inclusions. The obtained values are quite different in the two levels being −19 to −21‰ in the upper and −80‰ in the lower zone. The combined oxygen and hydrogen isotope composition of the fluid plots in the field of the metamorphic waters in the upper zone and in the lower δD limit of the magmatic water field in the lower zone (fields defined by Sheppard 1986). Variations in the hydrogen isotope composition in excess of 25‰ may be observed in a single deposit. These variations can be produced during fluid immiscibility (Kerrich 1987; Taylor 1997) and by changes in the oxygen fugacity of the fluid at the depositional site due to the hydrogen isotope fractionation between water and reduced species such as CH_4 and/or H_2 (Colvine et al. 1988). However, the difference observed at Serrinha appears to be too large to account for these processes. Alternatively, low δD values may also be produced by the influx of meteoric water during regional uplift (Goldfarb et al. 1993) and H_2 diffusion into inclusion cavities during deformation (e.g., Hall et al. 1991). Influx of meteoric water is unlikely because an accompanying lowering of the $\delta^{18}O$ values is expected in this case and mixing of fluids can be discarded based on the fluid inclusion study. On the other hand, the possibility of postentrapment modification (selective water leakage) was discussed for the lower mineralized level and this could remain a valid speculation for the low δD "magmatic" value. In addition, a causative magmatic event that could be responsible for the magmatic contribution is not known in the region. Furthermore, it is noteworthy that the "metamorphic values" found in Serrinha fall within the range of values estimated for the ore fluid in the Cachoeira deposit, which were interpreted to be derived from metamorphic sources (Klein et al. 2005a). In conclusion, there is no simple explanation for the observed large difference in the hydrogen isotope composition of the fluids in the upper and lower mineralized levels at Serrinha and none of the values can be a priori discarded nor assumed as the unique valid value. Nevertheless, deep-seated metamorphic and/or magmatic and/or mantle sources appear to be a reasonable inference for the ore-bearing fluid at Serrinha.

The carbon isotope composition of fluid CO_2 was estimated from the carbonate and graphite analysis using the calcite-, dolomite-, and graphite-CO_2 fractionation factors of Ohmoto and Rye (1979). The fluid $\delta^{13}C$ values of calcite and dolomite are nearly identical in the lower level, varying between −13.3 and −13.6‰, while the values of calcite in the upper level are slightly less negative (−11.9 to −12.1‰). The $\delta^{13}C$ values of CO_2 in equilibrium with graphite of the host rock are in the range of −10.6 to −11.0‰. The $\delta^{13}C$ value measured directly in the inclusion CO_2 is −17.6‰. The estimated carbon isotope compositions of the fluid CO_2 are distinct for carbonates, graphite, and fluid inclusions. These differences could imply fluids with different temperatures, which is unlikely, as indicated

Table 3 Calculated isotopic compositions of the fluid in equilibrium with hydrothermal minerals and graphite

Level	Mineral	$\delta^{18}O_{H2O}$ (‰)	δD_{H2O} (‰)	$\delta^{13}C_{CO2}$ (‰)	$\delta^{34}S_{H2S}$ (‰)
Upper level					
175	Quartz	+7.2 to +8.0			
175	Calcite	+13.9 to +14.6		−11.9 to −12.1	
175	Ankerite	+9.2 to +9.9			
175	Graphite			−10.6 to −10.7	
175	Pyrite				−3.8
176	Quartz	+6.2 to +7.0			
175/176	Fi*		−19 to −21		
Lower level					
206	Quartz	+6.9 to +7.7			
206	Fi[a]		−80	−17.6	
206	Calcite	+7.0 to +7.7		−13.4 to −13.6	
206	Dolomite	+7.7 to +8.4		−13.3 to −13.6	
206	Graphite			−10.9 to −11.0	
206	Pyrite				−9.1

[a]Fluid inclusion

by the previous discussion, or that carbonates precipitated from fluids having different composition than that of the fluid trapped in the fluid inclusions. However, considering the strongly negative $\delta^{13}C$ values found in the graphite samples and the isotopic equilibrium (quartz-carbonate, carbonate-carbonate) described at least for the lower level, it is more probable that the $\delta^{13}C$ values of the CO_2 in equilibrium with carbonates and of the fluid inclusion CO_2 are reflecting variable contribution of the ^{13}C-depleted carbon present in the host rocks. Therefore, the original isotopic values of carbon in fluid CO_2 might have been less negative than these calculated values (>−11‰). One could assume that the $\delta^{13}C$ values of the CO_2 in equilibrium with graphite would represent the carbon isotopic composition of the fluid. However, graphite was not in equilibrium with the fluid CO_2 or with the carbonates because the measured isotopic compositions would imply temperatures between 380 and ~550°C (Ohmoto and Rye 1979; Chacko et al. 1991). As a consequence, it is difficult to evaluate the original composition of the carbon in the fluid and its ultimate source. The strongly negative values of the graphite carbon clearly reflect an organic origin, whereas the original carbon isotope composition is compatible with mantle, magmatic, or metamorphic carbon (or their mixtures), i.e., a deep-seated source.

The $\delta^{34}S$ value of the fluid calculated from the $\delta^{34}S$ values of pyrite and the pyrite-H_2S fractionation factor of Ohmoto and Rye (1979) are −3.8 and −9.1‰ for the upper and lower zones, respectively, assuming H_2S as the main sulfur species in the fluid, which is compatible with the calculated redox conditions. Most of the deposits having geologic, mineralogical, and fluid characteristics similar to those presented in this study show $\delta^{34}S$ values in the range of −1 to +10‰. This is, in general, interpreted to reflect crustal average or a magmatic origin (Taylor 1987; McCuaig and Kerrich 1998, and references therein). Some deposits showed more negative $\delta^{34}S$ values that were ascribed to the involvement of oxidized fluids or oxidation of the hydrothermal fluid through intense interaction with host rocks that have sulfate minerals and/or hematite present in the alteration (Lambert et al. 1984; Phillips et al. 1986; Cameron and Hattori 1987) or to the influence of sedimentary-diagenetic sulfides present in host rocks (Oberthür et al. 1996). None of these features were identified in this study. Significant fluid immiscibility and consumption of CO_2 to form carbonate or trapped in fluid inclusions, which were all documented at Serrinha, may also lead to oxidation of the residual fluid (Drummond and Ohmoto 1985).

Geologic–genetic model for the Serrinha deposit

The Serrinha gold deposit in the Gurupi Belt is hosted by highly strained graphite-bearing schists developed within the Tentugal shear zone. The schists belong to a Paleoproterozoic orogenic metavolcano-sedimentary sequence formed in an island arc/continental margin setting. The ore-zones are discontinuous and boudinaged, concordant with the foliation of the host rock, and are characterized by quartz-carbonate veins and weak concentrations of pyrite both in the veins and in the host rock. The quartz-carbonate veins are locally laminated and show microscopic evidence of heterogeneous deformation from recrystallization to brittle fracturing. Collectively, the textural and structural data indicate that mineralization was syn- to late-tectonic and postmetamorphic and that opening of the foliation planes played a fundamental role in concentrating the mineralization.

Genetic relationships can be deduced from mineralogical, fluid inclusion and stable isotope data. Fluid inclusion studies revealed early CO_2-(±CH_4-N_2) and CO_2-(±CH_4-N_2)-H_2O-NaCl inclusions and subordinate postore H_2O-NaCl inclusions. The carbon-bearing inclusions show highly variable phase ratios, CO_2 homogenization, and total homogenization temperatures both to liquid and vapor, interpreted as the product of fluid immiscibility under fluctuating pressure conditions, accompanied and/or followed by local reequilibration provoked by deformation of the host quartz. The low-salinity and moderately dense mineralizing fluid was trapped mostly between 310 and 335°C and between 1.3 and 3.0 kbar according to fluid inclusion homogenization temperatures and oxygen isotope thermometry. Considering that part of the early fluid inclusions occur in short trails within the host quartz, the mode of occurrence of gold, and the consistency of the temperatures obtained by different geothermometers, it is reasonable to assume that the early CO_2-bearing fluid inclusions represent the ore-bearing fluid.

The carbon, oxygen, and hydrogen isotopes data have not defined the ultimate source for the fluids but their origin are nonetheless restricted to metamorphic, magmatic, or mantle sources. As such, deep-seated sources are implied. Strongly negative carbon isotope compositions in graphite indicate organic contribution at the site of deposition and sulfur isotope data indicate some possible oxidation of the fluid.

Considering the estimated T–P conditions that pyrite is the main sulfide mineral in the alteration assemblage, the absence of oxidized minerals, the low salinity CO_2-rich fluid, the graphite-bearing host rocks, and the calculated fO_2 relatively reduced conditions are implied for the hydrothermal fluid at Serrinha. Under such conditions, $AuHS_2^-$ was likely the gold transporting complex (e.g., Benning and Seward 1996). The destabilization of this complex and the consequent precipitation of gold resulted from chemical changes in the transporting fluid at the depositional site. These changes at the physicochemical conditions estimated for Serrinha, were probably produced by fluid–rock interactions and phase separation, generally induced by pressure fluctuations (e.g., Robert et al. 1995; Mikucki 1998) accompanied by some oxidation of the fluid. Phase separation (immiscibility) of a CO_2-H_2O-rich fluid was documented in the fluid inclusion study and may be the main process responsible for the concentration of free gold in the veins. Furthermore, the removal of CO_2 from solution increases the pH of the solution and the activity of the carbonate ion in this solution causing the

precipitation of carbonate minerals (Rimstidt 1997). Desulfidation of the ore-bearing fluid by reaction with Fe-bearing minerals in the host rocks (magnetite and minor chlorite) causing changes in the redox conditions of the fluid, may have been responsible for the subordinate precipitation of the pyrite–gold assemblage. Although water/rock ratios could not be quantified in this study, the reactions occurred in a fluid-dominated system and under nearly isothermal conditions as inferred by the minimal variation in the fluid isotope compositions.

The geologic characteristics of the Serrinha deposit, namely, structure, host rocks (type, metamorphic grade), alteration mineralogy, mineralization style, timing of the mineralization with respect to deformation and metamorphism, and suggested tectonic setting, along with the fluid and stable isotope data, indicate that Serrinha belongs to the class of orogenic gold deposits in the sense of Groves et al. (1998), analogous to other deposits in the Gurupi Belt.

Acknowledgements This study was funded by CAPES (BEX 2020/02-05), CPRM/Geological Survey of Brazil, and Universidade Federal do Pará (UFPA) and constitutes a contribution to the project PRONEX/CNPq/UFPA (66.2103/1998). C. Torresini, G. M. Brandão, M. A. Ferreira, and J. W. A. Ribeiro (formerly Mineração Santa Fé) are gratefully acknowledged for field support for providing access to the drill cores and for discussions on the deposit geology. Photo 4D is courtesy of J. W. A. Ribeiro. C. N. Lamarão (UFPA) kindly helped with the SEM images. Constructive comments and suggestions of Steffen Hagemann, Larry Meinert and an anonymous reviewer, as well as the editorial handling of Hartwig Frimmel are greatly appreciated.

References

Al-Assam IS, Taylor BE, South BS (1990) Stable isotope analysis of multiple carbonate samples using selective acid extraction. Chem Geol Isot Geosc Sect 80:119–125

Almeida FFM, Melcher GC, Cordani UG, Kawashita K, Vandoros P (1968) Radiometric age determinations from northern Brazil. Boletim Soc Bras Geol 17:3–14

Anderson MR, Rankin AH, Spiro B (1992) Fluid mixing in the generation of mesothermal gold mineralization in the Transvaal sequence, Transvaal, South Africa. Eur J Mineral 4:933–948

Araujo Neto H (1998) Programa Nacional de Prospecção de Ouro—PNPO. Mapa de reserves e produção de ouro doBrasil. CPRM, Brasília

Benning LG, Seward TM (1996) Hydrosulphide complexing of Au (I) in hydrothermal solutions from 150 to 400°C and 500 to 1,500 bars. Geochim Cosmochim Acta 60:1849–1871

Bowers TS, Helgeson HC (1983) Calculation of the thermodynamic and geochemical consequences of nonideal mixing in the system H_2O-CO_2-NaCl on phase relations in geological systems: equation of state for H_2O-CO_2-NaCl fluids at high pressures and temperatures. Geochim Cosmochim Acta 47:1247–1275

Brown PE (1989) Flincor: a microcomputer program for the reduction and investigation of fluid inclusion data. Am Mineral 74:1390–1393

Burke EAJ (2001) Raman microspectrometry of fluid inclusions. Lithos 55:139–158

Cameron EM, Hattori K (1987) Archean gold mineralization and oxidized hydrothermal fluids. Econ Geol 82:1177–1191

Cathelineau M, Marignac C (1994) Use of fluid inclusions for a better understanding of intracontinental geothermal activities. In: De Vivo B, Frezzotti ML (eds) Fluid inclusions in minerals: methods and applications. Virginia Tech, Blacksburg, pp 309–326

Chacko T, Mayeda TK, Clayton RN, Goldsmith JR (1991) Oxygen and carbon isotope fractionations between CO_2 and calcite. Geochim Cosmochim Acta 55:2867–2882

Chiba H, Chacko T, Clayton RN, Goldsmith JR (1989) Oxygen isotope fractionations involving diopside, forsterite and calcite: applications to geothermometry. Geochim Cosmochim Acta 53:2985–2995

Coleman ML, Shepherd TJ, Durham JJ, Rouse JE, Moore GR (1982) Reduction of water with zinc for hydrogen isotope analysis. Anal Chem 54:993–995

Collins PLF (1979) Gas hydrates in CO2-bearing fluid inclusions and the use of freezing data for estimation of salinity. Econ Geol 74:1435–1444

Colvine AC, Fyon JA, Heather KB, Marmont S, Smith PM, Troop DG (1988) Archean lode gold deposits in Ontario. Ont Geol Surv Misc Pap 139:136

Crawford ML, Hollister LS (1986) Metamorphic fluids: the evidence from fluid inclusions. In: Walther JV, Wood BJ (eds) Fluid rock interaction during metamorphism. Physical Geochemistry, vol 5. Springer, Berlin Heidelberg New York, pp 1–35

Diamond L (1994) Salinity of multivolatile fluid inclusions determined from clathrate hydrate stability. Geochim Cosmochim Acta 58:19–41

Diamond L (2001) Review of the systematics of CO_2-H_2O fluid inclusions. Lithos 55:69–99

Drummond SE, Ohmoto H (1985) Chemical evolution and mineral deposition in boiling hydrothermal systems. Econ Geol 80:126–147

Dubessy J (1994) Single components systems: phase diagrams and their application to fluid inclusions. In: De Vivo B, Frezzotti ML (eds) Fluid inclusions in minerals: methods and applications. Virginia Tech, Blacksburg, pp 95–115

Dugdale AL, Hagemann SG (2001) The Bronzewing lode–gold deposit, Western Australia: P-T-X evidence for fluid immiscibility caused by cyclic decompression in gold-bearing quartz-veins. Chem Geol 173:59–90

Fonarev VI, Touret JLR, Kotelnikova ZA (1998) Fluid inclusions in rocks from the Central Kola granulite area (Baltic Shield). Eur J Mineral 10:1118–1120

Frantz JD, Popp RK, Hoering TC (1992) The compositional limits of fluid immiscibility in the system H_2O-NaCl-CO_2 as determined with the use of synthetic fluid inclusions in conjunction with mass spectrometry. Chem Geol 98:237–255

Friedman I, O'Neil JR (1977) Compilation of stable isotope fractionation factors of geochemical interest. US Geol Surv Prof Pap 440-KK:1–12

Goldfarb RJ, Snee LW, Pickthorn WJ (1993) Orogenesis, high-T thermal events, and gold vein formation within metamorphic rocks of the Alaskan Cordillera. Mineral Mag 57:375–394

Goldstein RH, Reynolds TJ (1994) Systematics of fluid inclusions in diagenetic minerals. SEPM Short Course 31:1–198

Groves DI, Goldfarb RJ, Gebre-Mariam M, Hagemann SG, Robert F (1998) Orogenic gold deposits: a proposed classification in the context of their crustal distribution and relationship to other gold deposit types. Ore Geol Rev 13:7–27

Hagemann SG, Brown PE (1996) Geobarometry in Archean lode–gold deposits. Eur J Mineral 8:937–960

Hall DL, Bodnar RJ, Craig JR (1991) Evidence for post-entrapment diffusion of hydrogen into peak metamorphic fluid inclusions from the massive sulfide deposits at Ducktown, Tennessee. Am Mineral 76:1344–1355

Harris C, Stuart Smith H, le Roex AP (2000) Oxygen isotope composition of phenocrysts from Tristan da Cunha and Gough island lavas: variation with fractional crystallization and evidence for assimilation. Contrib Mineral Petrol 138:164–175

Hendel EM, Hollister IS (1981) An empirical solvus for CO_2-H_2O-2.6 wt % salt. Geochim Cosmochim Acta 45:225–228

Henley RW, Truesdell AH, Barton PB Jr, Whitney JA (1984) Fluid mineral equilibria in hydrothermal systems. Rev Econ Geol 1:267

Huizenga JM, Touret JLR (1999) Fluid inclusions in shear zones, the case of the Umwindsi shear zone in the Harare–Shamva–Bindura greenstone belt, NE Zimbabwe. Eur J Mineral 11:1079–1090

Hurley PM, Melcher GC, Pinson WH, Fairbairn HW (1968) Some orogenic episodes in South America by K-Ar and whole-rock Rb-Sr dating. Can J Earth Sci 5:633–638

Kerrich R, (1987) The stable isotope geochemistry of Au-Ag vein deposits in metamorphic rocks. In: Kyser TK (ed) Stable isotope geochemistry of low temperature fluids. Mineral Assoc Canada, Short Course 13:287–336

Klein EL, Moura CAV (2001) Age constraints on granitoids and metavolcanic rocks of the São Luis craton and Gurupi belt, northern Brazil: implications for lithostratigraphy and geological evolution. Int Geol Rev 43:237–253

Klein EL, Moura CAV (2003) Sintese geológica e geocronológica do Craton São Luís e do Cinturão Gurupi na região do rio Gurupi (NE-Para/NW-Maranhão). Rev Geol USP Série Cient 3:97–112

Klein EL, Harris C, Giret A, Moura CAV, Angélica RS (2005a) Geology and stable isotope (O, H, C, S) constraints on the genesis of the Cachoeira gold deposit, Gurupi Belt, northern Brazil. Chem Geol 221:188–206

Klein EL, Moura CAV, Pinheiro BLS (2005b) Paleoproterozoic crustal evolution of the São Luís Craton, Brazil: evidence from zircon geochronology and Sm-Nd isotopes. Gondwana Res 8:177–186

Klein EL, Moura CAV, Krymsky RS, Griffin WL (2005c) The Gurupi belt, northern Brazil: lithostratigraphy, geochronology, and geodynamic evolution. Precambrian Res 141:83–105

Kyser TK (1987) Equilibrium fractionation factors for stable isotopes. In: Kyser TK (ed) Short course in "stable isotope geochemistry of low temperature fluids", vol 13. Mineralogical Association of Canada short course handbook, pp 1–84

Lambert IB, Phillips GN, Groves DI (1984) Sulfur isotope compositions and genesis of Archaean gold mineralization, Australia and Zimbabwe. In: Foster RP (ed) Gold '82: the geology, geochemistry and genesis of gold deposits, Geol Soc Zimb 1:373–387 (special pub)

Loucks RR (2000) Precise geothermometry on fluid inclusion populations that trapped mixtures of immiscible fluids. Am J Sci 300:23–59

Marcoux E, Milési JP (1993) Lead isotope signature of Early Proterozoic ore deposits in Western Africa: comparison with gold deposits in French Guiana. Econ Geol 88:1862–1879

Matsuhisa Y, Goldschmit JR, Clayton RN (1979) Oxygen isotope fractionation in the system quartz-albite-anorthite-water. Geochim Cosmochim Acta 43:1131–1140

McCuaig TC, Kerrich R (1998) P-T-t-deformation-fluid characteristics of lode gold deposits: evidence from alteration systematics. Ore Geol Rev 12:381–453

McRea M (1950) The isotopic chemistry of carbonates and a paleotemperature scale. J Chem Phys 18:849–857

Mikucki E (1998) Hydrothermal transport and depositional processes in Archaean lode–gold systems: a review. Ore Geol Rev 13:307–321

Naden J, Shepherd TJ (1989) Role of methane and carbon dioxide in gold deposition. Nature 342:793–795

Oberthür T, Schmidt-Mumm A, Vetter U, Simon K, Amanor JA (1996) Gold mineralization in the Ashanti Belt of Ghana: genetic constraints of the stable isotope geochemistry. Econ Geol 91:289–301

Oberthür T, Vetter U, Davis DW, Amanor JA (1998) Age constraints on gold mineralization and Paleoproterozoic crustal evolution in the Ashanti belt of southern Ghana. Precambrian Res 89:129–143

Ohmoto H, Kerrick D (1977) Devolatilization equilibria in graphitic systems. Am J Sci 277:1013–1044

Ohmoto H, Rye RO (1979) Isotopes of sulfur and carbon. In: Barnes HL (ed) Geochemistry of hydrothermal ore deposits. Wiley, New York, pp 509–567

Ohmoto H, Goldhaber MB (1997) Sulfur and carbon isotopes. In: Barnes HL (ed) Geochemistry of hydrothermal ore deposits. Wiley, New York, pp 517–611

Palheta ESM (2001) Evolução geológica da região nordeste do Estado do Pará com base em estudos estruturais e isotópicos de granitóides. MSc thesis, Universidade Federal do Pará, Belém, Brazil

Phillips GN, Groves DI, Neall FB, Donnelly TH, Lambert IB (1986) Anomalous sulphur isotope compositions in the Golden Mile, Kalgoorlie. Econ Geol 81:2008–2015

Ramboz C, Pichavant M, Weisbrod A (1982) Fluid immiscibility in natural processes: use and misuse of fluid inclusion data. II. Interpretation of fluid inclusion data in terms of immiscibility. Chem Geol 37:29–48

Ribeiro JWA (2002) O arcabouço estrutural da região de Chega Tudo e Cedral, NW do Maranhão, com base em sensores geofisicos. MSc thesis. Universidade Federal do Pará, Belém, Brazil

Rimstidt JD (1997) Gangue mineral transport and deposition. In: Barnes HL (ed) Geochemistry of hydrothermal ore deposits. Wiley, New York, pp 487–515

Robert F, Boullier AM, Firdaous K (1995) Gold-quartz veins in metamorphic terranes and their bearing on the role of fluids in faulting. J Geophys Res 100(B7):12861–12879

Roedder E (1984) Fluid inclusions. Rev Miner 12:644

Rosenbaum J, Sheppard SMF (1986) An isotopic study of siderites, dolomites and ankerites at high temperatures. Geochim Cosmochim Acta 50:1147–1150

Ryzhenko BN, Volkov VP (1971) Fugacity coefficients of some gases in a broad range of temperature and pressures. Geochem Int 8:468–481

Seitz JC, Pasteris JD (1990) Theoretical and practical aspects of differential partitioning of gases by clathrate hydrates in fluid inclusions. Geochim Cosmochim Acta 54:631–639

Shepherd TJ, Rankin AH, Alderton DH (1985) A practical guide for fluid inclusion studies. Blackie, Glasgow

Shepherd TJ, Bottrell SH, Miller MF (1991) Fluid inclusion volatiles as an exploration guide to black shale-hosted gold deposits, Dollgelau gold belt, North Wales, UK. J Geochem Explor 42:5–24

Sheppard SMF (1986) Characterization and isotopic variations in natural waters. In: Valley JW, Taylor HP, O'Neil JR (eds) Stable isotopes in high temperature geological processes. Rev Miner 16:165–183

Sheppard SMF, Schwarcz HP (1970) Fractionation of carbon and oxygen isotopes and magnesium between coexisting metamorphic calcite and dolomite. Contrib Mineral Petrol 26: 161–198

Sibson RH (1990) Faulting and fluid flow. In: Nesbitt BE (ed) Short course on "fluids in tectonically active regimes of the continental crust", vol 18. Mineralogical Association of Canada short course handbook, pp 92–132

Spicuzza MJ, Valley JW, Kohn MJ, Girard JP, Fouillac AM (1998) The rapid heating, defocused beam technique: a CO_2-laser-based method for highly precise and accurate determination of $\delta^{18}O$ values of quartz. Chem Geol 144:195–203

Taylor BE (1987) Stable isotope geochemistry of ore-forming fluids. In: Kyser TK (ed) Short course in "stable isotope geochemistry of low temperature fluids", vol 13. Mineralogical Association of Canada short course handbook, pp 337–445

Taylor HP (1997) Oxygen and hydrogen isotope relationships in hydrothermal mineral deposits. In: Barnes HL (ed) Geochemistry of hydrothermal ore deposits, 3rd edn. Wiley, New York, pp 229–302

Torresini C (2000) The Gurupi gold deposits (Cipoeiro and Chega Tudo), Gurupi Belt, Pará, Brazil; geology and mineralization. International Gold Symposium, 4, Lima, Peru, Anals. Sociedade Peruana de Geologia (on CD-ROM)

Touret JLR (2001) Fluids in metamorphic rocks. Lithos 55:1–25

Van den Kerkhof AM, Hein UF (2001) Fluid inclusion petrography. Lithos 55:27–47

Van den Kerkhof AM, Thiéry R (2001) Carbonic inclusions. Lithos 55:49–68

Villas RNN (1982) Geocronologia das intrusões ígneas na bacia do rio Guamá, nordeste do Estado do Pará. Simpósio de Geologia da Amazônia, 2, Anals, vol 1. pp 233–247

Vityk MO, Bodnar RJ (1995) Textural evolution of fluid inclusions in quartz during reequilibration, with applications to tectonic reconstruction. Contrib Mineral Petrol 121:309–323

Wilkins RWT, Barkas JP (1978) Fluid inclusions, deformation and recrystallization in granite tectonites. Contrib Mineral Petrol 65:293–299

Yamaguti HS, Villas RNN (2003) Estudo microtermométrico dos fluidos hidrotermais relacionados com a mineralização aurífera de Montes Áureos, NW do Maranhão. Rev Bras Geociênc 33:21–32

Zheng YF (1999) Oxygen isotope fractionations in carbonate and sulfate minerals. Geochem J 33:109–126